

RESEARCH ARTICLE | MAY 22 2023

Comparing the kinetics of ionized and neutral atoms from single and multi-element laser-produced plasmas

Elizabeth J. Kautz ; Mark C. Phillips ; Prasoon K. Diwakar ; Alla Zelenyuk ; Sivanandan S. Harilal 

 Check for updates

Phys. Plasmas 30, 052106 (2023)

<https://doi.org/10.1063/5.0146958>



View
Online



Export
Citation

11 April 2024 20:08:11

AIP Advances

Why Publish With Us?



25 DAYS
average time
to 1st decision



740+ DOWNLOADS
average per article



INCLUSIVE
scope

[Learn More](#)

Comparing the kinetics of ionized and neutral atoms from single and multi-element laser-produced plasmas

Cite as: Phys. Plasmas **30**, 052106 (2023); doi: 10.1063/5.0146958

Submitted: 17 February 2023 · Accepted: 2 May 2023 ·

Published Online: 22 May 2023



View Online



Export Citation



CrossMark

Elizabeth J. Kautz,^{1,2,a)}  Mark C. Phillips,³  Praseon K. Diwakar,⁴  Alla Zelenyuk,² 
and Sivanandan S. Harilal^{2,5} 

AFFILIATIONS

¹Nuclear Engineering Department, North Carolina State University, Raleigh, North Carolina 27695, USA

²Pacific Northwest National Laboratory, Richland, Washington 99352, USA

³James C. Wyant College of Optical Sciences, University of Arizona, Tucson, Arizona 85721, USA

⁴South Dakota School of Mines and Technology, Rapid City, South Dakota 57701, USA

⁵Chemistry Department, Washington State University, Pullman, Washington 99164, USA

^{a)} Author to whom correspondence should be addressed: ekautz@ncsu.edu

ABSTRACT

Kinetics of ion and neutral atom emission features were compared for nanosecond laser-produced plasmas generated from several metal targets (i.e., Al, Ti, Zr, Nb, Ta) and an alloy containing all of these as principal alloying elements. Plasmas were produced by focusing 6 ns, 1064 nm pulses from an Nd:YAG laser on the targets of interest in a vacuum. A Faraday cup was used for collecting ion temporal features while spatially and temporally resolved emission spectroscopy was used for measuring the optical time of flight of various neutral atomic transitions. Our results highlight that most probable ion and atom velocities decay with increasing atomic mass. Trends for ions from the alloy target represent a weighted average where all ions contribute. For both ions and atoms, velocities decrease with increasing heat of vaporization and melting temperature, consistent with the thermal mechanisms that contribute to nanosecond laser ablation. Kinetic energies for neutral atoms from pure metal targets have some variability with atomic mass, whereas kinetic energies for atoms from the alloy target are more similar. These more similar kinetic energies observed for neutral atoms in the multi-element plasma may be attributed to collisions between species from all elements in the Knudsen layer.

Published under an exclusive license by AIP Publishing. <https://doi.org/10.1063/5.0146958>

I. INTRODUCTION

Laser-produced plasmas (LPPs) are used in numerous applications, including light sources, machining, material processing, thin-film deposition, elemental analysis, particle generation, and remote sensing.^{1–4} One of the key advantages of LPPs is the large parametric space available for fine tuning the LPP properties for different applications. Typically, high-density and low-temperature (≈ 1 eV) LPPs are used for analytical applications (e.g., laser-induced breakdown spectroscopy or LIBS⁵) where atomic spectral emission features are used for elemental detection and quantification. In contrast, low-density and high-temperature plasmas (≈ 30 eV) are preferred for light sources for extreme ultraviolet (EUV) lithography.⁶ Plasmas with such a wide range of physical properties are generated by optimizing LPP parameters that are monitored using various plasma diagnostics.

Plasma diagnostics play a central role in understanding fundamental properties of LPPs.^{1,7} For instance, the kinetic distribution of electrons and ions emanating from an LPP source is regularly measured using Faraday cups and Langmuir probes.^{8–11} Faraday cups have been used to analyze ions in LPPs since the 1970s^{12,13} and are a well-known device for measuring absolute ion beam intensities and their kinetics. Hence, Faraday cups are used as ion collectors in laser ablation (LA)-based mass spectroscopy analytical instrumentation.¹⁴ In addition, optical emission spectroscopy (OES) is one of the most commonly used methods among all plasma diagnostic tools because of its passive nature and experimental simplicity.¹ Spatially and temporally resolved OES is a useful method for studying the kinetics of emitting species in LPPs.^{15,16} Optical time of flight (OTOF) is also a useful tool for understanding the kinetics of the excited population of

ionic (charged) species¹⁰ in addition to atomic and molecular (neutral) species in the plume.^{17,18}

Nanosecond (ns) duration lasers are regularly used for producing plasmas where thermal processes are dominant due to the relatively long duration of the laser pulse compared to characteristic energy transfer (electrons to ions) and heat conduction times. Previous results highlighted that the ion emission from a metal target showed a conical feature due to a preferential emission along the target normal direction.¹⁹ Other studies showed that the angular distribution of ions followed an approximately single charge-dependent, \cos^n function, where n increases with charge state and decreases with atomic mass.²⁰ The space charge effect of the charged particles in the plasma results in increasing ion velocity for higher charge states.²¹

The kinetics of LPP plumes are influenced by laser, target, and environmental (e.g., nature and pressure of the ambient gas) properties. Many studies evaluated the role of laser wavelength, pulse width, and power density on plasma dynamics.^{9,10,21,22} Similarly, a large number of studies investigated the role of ambient gas type (e.g., Ar, O₂, air) and pressure on the plume dynamics and plasma chemistry.^{23–25} While some work exists on understanding the role of target properties on the kinetics of the LPP plume,^{9,22,26,27} the comparison of charged and neutral species has received less attention. In addition, studies involving targets with multiple principal elements are relatively limited.^{28–30}

Plasma diagnostics have been used extensively in the context of pulsed laser deposition (PLD) in order to understand dynamics of plume species and plasma properties (i.e., temperature, electron density) for optimizing film characteristics.³¹ However, optimization of the plasma properties and stoichiometric deposition is more challenging for multi-element LPPs and reactive thin film deposition which require further study.³⁰ In addition, multi-principal element and high entropy alloy thin films have been fabricated via PLD; however, the focus of several prior works has been on the film itself (e.g., microstructure, composition, properties),^{32,33} as opposed to the plasma kinetics.

This article compares the dynamics of ionized and neutral atoms from pure metal vs alloy target materials. LPPs were generated via ns LA of Al, Ti, Zr, Nb, and Ta targets, and a refractory-based alloy containing all of these as principal elements. A Faraday cup was used as an ion collector for determining the ion kinetic energy (KE) distributions. Spatially resolved OTOF was performed to identify the velocity and KE distributions of atoms. Combining these two techniques, we explore the relationship between the kinetics of ionic and atomic emission features and thermophysical properties of single element and alloy target materials.

II. EXPERIMENTAL DETAILS

A schematic of the experimental setup is given in Fig. 1. For producing plasmas, pulses from an Nd:YAG laser [1064 nm wavelength, ≈ 6 ns full-width half maximum (FWHM)], with a laser fluence of ≈ 20 J/cm² (power density of 3.4×10^9 W cm⁻²), were focused on to various targets at normal incidence. The targets were positioned in a vacuum chamber and mounted on an x–y translator to easily move between targets and prevent drilling. Multiple optical windows and ports for laser entrance, light collection, and electronics were included in the chamber design. Target materials used in this study include pure Al, Ti, Zr, Nb, and Ta (99.9% purity, Kurt Lesker), and a

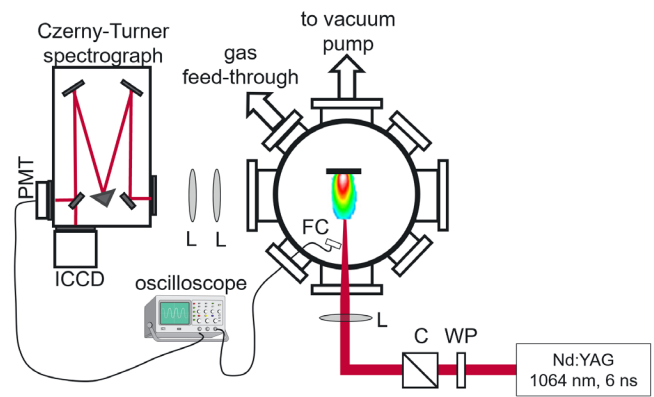


FIG. 1. Schematic of the experimental setup used for collecting time and spatially resolved OTOF and Faraday cup ion signals. Acronyms are defined as follows: PMT—photomultiplier tube, ICCD—intensified charged coupled device, L—lens, FC—Faraday cup, M—mirror, C—cube polarizer, WP—wave plate.

refractory high entropy alloy (RHEA) with 10% Al, 30% Ti, 20% Zr, 20% Nb, 15% Ta, 5% V (in at. %).^{34,35} This alloy was selected for this study given Al, Ti, Zr, Nb, and Ta are all principal alloying elements in amounts above 10 at. %.

A Faraday cup ion collector with a 3 mm entrance aperture was placed ≈ 18 cm from the target at an angle of $\approx 10^\circ$ for monitoring ions in LPPs. A -30 V bias voltage was applied to the ion collector, and the ion signal was acquired using an 1 GHz oscilloscope.

Spatially and temporally resolved OTOF emission spectroscopy was used for analyzing the kinetics of neutral species. For this, an optical system consisting of two plano-convex lenses was used for imaging the plasma plume onto the slit of a 0.5 m spectrograph (Spectrapro 2500i, Princeton Instruments) positioned orthogonal to the plasma expansion direction. The light dispersing system is equipped with two detectors: (i) a photomultiplier tube (PMT, Hamamatsu R955) with a ≈ 2 ns rise time and (ii) an intensified CCD (ICCD). The monochromator-PMT system was used for measuring the OTOF of various species in the plume at a specific distance from the target. The spectrograph entrance slit width used for data collection was $30 \mu\text{m}$, and slit height was ≈ 3 mm. The sampled region of the plasma is, therefore, small relative to the overall plume size. All analyses were carried out at a base pressure better than 1×10^{-7} Torr.

III. RESULTS

Ion emission from Al, Ti, Zr, Nb, and Ta pure metal targets was investigated and compared to ion emission from an alloy target containing all of these elements. The TOF ion profiles and KE distributions from the various metal and alloy targets are given in Figs. 2(a) and 2(b), respectively. In Fig. 2(a), all normalized ion profiles are fitted with a shifted Maxwell-Boltzmann (SMB) equation,³⁶ where fits are shown as dashed lines in each sub-figure. Velocity and KE temporal distributions were measured from the TOF profiles based on the atomic mass of each element and the location of the detector (18 cm from the target).

In Fig. 2(a) ion TOF profiles, we find a prompt peak is present at the onset of laser ablation for all targets. We also find that the FWHM and the probable arrival time (i.e., peak delay) both increase with target atomic mass, from Al to Ta. These TOF profiles follow an

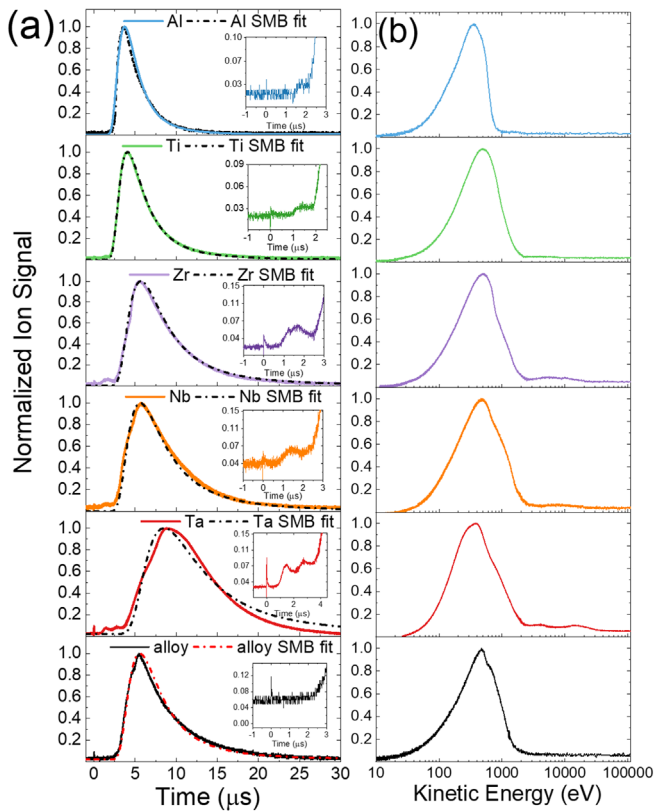


FIG. 2. (a) Ion TOF signal for Al, Ti, Zr, Nb, and Ta ions (from pure metal targets) and from the alloy target. Insets for each sub-figure are for early times. The dashed lines in (a) show the SMB fit to the ion profile data. Relative standard deviation (RSD) for SMB fits are 0.97 (Al), 0.99 (Ti), 0.99 (Zr), 0.98 (Nb), 0.96 (Ta), and 0.94 (alloy). (b) Ion signal as a function of KE. All signals in (a) and (b) are normalized to their maximum intensity.

approximate SMB distribution (indicating ions are thermalized), which is clear from the SMB fits reported in Fig. 2(a). Finally, several low-intensity ion peaks are observed at early times ($\approx 1\text{--}2\ \mu\text{s}$ for Al, Ti, Zr, Nb, and $\approx 1\text{--}4\ \mu\text{s}$ for Ta), as seen in the insets in Fig. 2(a). Such peaks are absent in the alloy profile.

All ion TOF profiles showed a presence of a prompt peak at $\approx 0\text{ ns}$, and the origin of prompt peaks has previously been attributed to photo-ionization caused by high-energy photons.^{37,38} From the ion profiles reported in Fig. 2, the maximum probable velocities of ions from each target material were calculated and are reported as a function of atomic mass in Fig. 3(a). The range of velocities at FWHM of the corresponding velocity distributions is given as a thick, shaded bar around the maximum probable value (given as a dark circle for pure target materials and a star for the alloy target).

Maximum probable KE for ions are given in Fig. 3(b), and KE distributions at FWHM are given as ranges. Errors associated with maximum probable velocities and kinetic energies reported here are $\leq 5\%$. The most probable ion velocity decreases with increasing atomic mass, as does the width of the velocity distribution. In terms of KE, the most probable values and widths of the distributions are similar for all elements; however, Al shows a reduced KE and width

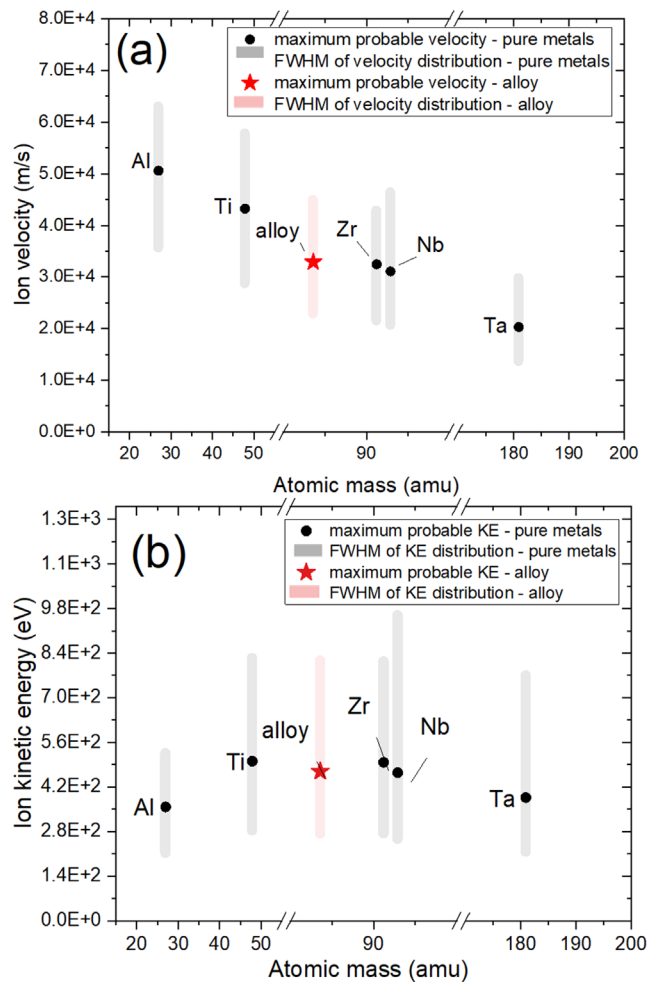


FIG. 3. (a) Maximum probable velocity of ions measured from Faraday Cup TOF profiles (Fig. 2) as a function of atomic mass (amu). Distributions around the maximum probable velocity data points represent the velocity distribution at FWHM, as noted in the figure caption. (b) Maximum probable KE as a function of atomic mass, including FWHM of KE distribution, plotted as a range. The atomic mass for the alloy target is estimated based on at. % and atomic mass of each alloying element.

relative to the other elements. Still, the measured energy range for Al falls within the ranges observed for the other elements.

Maximum probable ion velocities (and corresponding velocity ranges) are also plotted as a function of the heat of vaporization and melting temperature in Fig. 4. The melting temperature of the alloy target is reported in Ref. 35. The atomic mass and heat of vaporization for the alloy were estimated as weighted averages as a first approximation, given no experimental measurements on this new alloy are available in the literature. Figure 4 shows ion velocities decrease with increasing heat of vaporization and melting temperature. Velocities of all ions from the alloy target show good agreement with trends of ions in plasmas produced from pure target materials.

The OTOF profiles of selected atomic emission lines were measured at a distance of 6 mm from target surfaces. The 6 mm distance

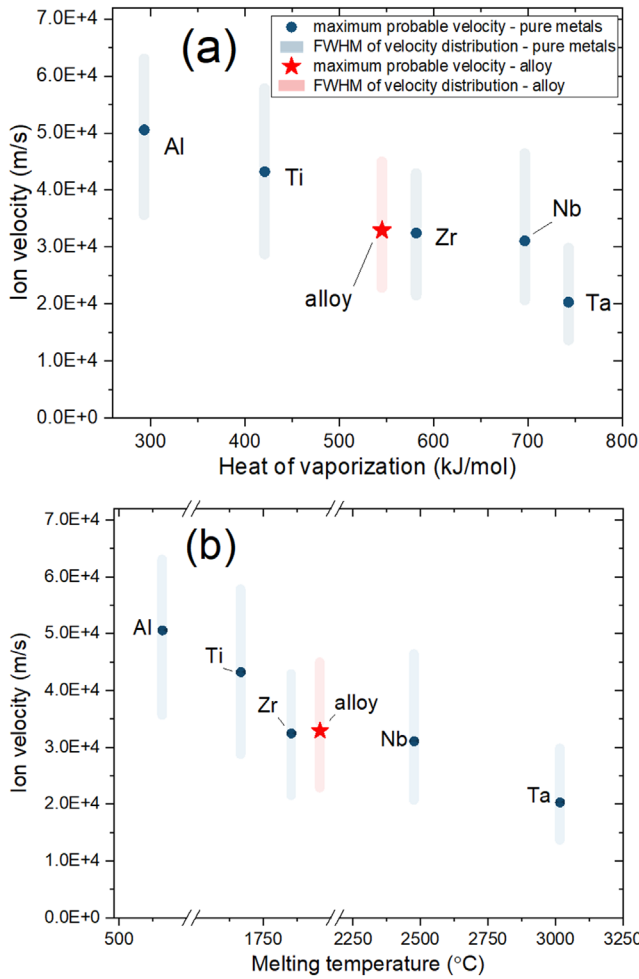


FIG. 4. Velocity of ions measured from Faraday Cup TOF profiles (Fig. 2) as a function of (a) heat of vaporization and (b) melting temperature. Distributions around the maximum probable velocity data points represent the velocity distribution at FWHM.

TABLE I. Atomic (neutral) transitions selected for OTOF measurements in pure and multi-element LPPs. Wavelength in vacuum (nm), upper energy level, lower energy level, and oscillator strength are given for each transition.³⁹

	Wavelength λ (nm)	Upper energy level E_k (cm^{-1})	Lower energy level E_i (cm^{-1})	Oscillator strength $\log(gf)$
Al I	256.7983	38 929.405	0	-1.06
Ti I	499.1065	26 772.969	6742.755	0.38
Zr I	270.6169	36 941.65	0	-0.83
Nb I	405.8926	25 680.36	1050.26	0.58
Ta I	648.5312	28 766.65	13 351.45	-0.46

was selected for investigation here where the plasma is expanding adiabatically and collisions are more significant at closer distances to the target surfaces. The selected transitions for OTOF studies are given in Table I.³⁹ The OTOF profiles recorded from metal and alloy targets are reported in Fig. 5(a), with KE distributions given in Fig. 5(b). In Fig. 5, solid colored lines represent profiles from pure metal targets, and dashed black lines are for the same transition but from the alloy target.

Each OTOF profile in Fig. 5(a) has a sharp, prompt peak at early times (near $\approx 0 \mu\text{s}$) and a broader peak at later times. The prompt emission signal noticed in OTOF profiles is contributed by continuum emission which peaks at very early times after the plasma onset.¹ The OTOF profiles for each atomic transition showed different trends for the pure metal vs alloy targets. For example, the peak in the Al I

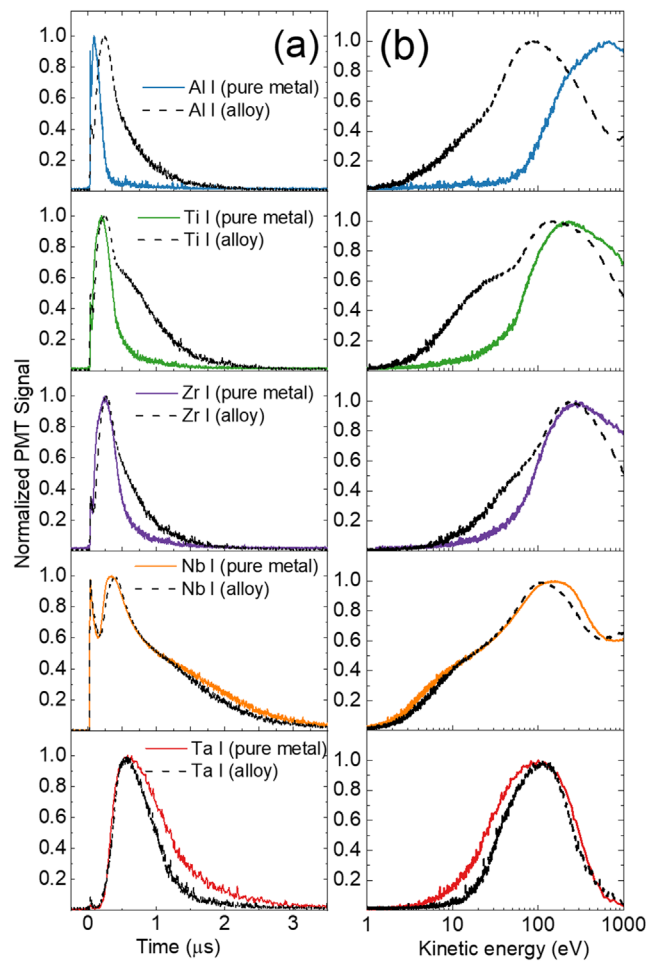


FIG. 5. (a) OTOF profiles for Al, Ti, Zr, Nb, and Ta neutral atoms in plasmas produced from pure metal and alloy targets (b) and corresponding KE distributions. KE distributions are given up to 1000 eV, given the difficulty in separating the signal corresponding to atomic emission with the prompt peak. OTOF signals for neutral atoms from pure metal targets are given as solid, colored lines, and neutral atoms from the alloy target are shown as dashed black lines. All signals are taken at 6 mm from targets. Atomic transitions selected are Al I at 256.7983 nm, Ti I at 499.1065 nm, Zr I at 270.6169 nm, Nb I at 405.8926 nm, and Ta I at 648.5312 nm.

OTOF profile for the alloy is delayed relative to the pure metal target. In contrast, for heavy metals such as Nb I and Ta I, there is less difference between the profiles from pure metal and alloy targets. For Al I, Ti I, and Zr I, the alloy target shows a longer decay curve in the OTOF profiles when compared to the pure metal targets. Differences apparent in OTOF profiles are also observed in the PMT signals plotted as a function of KE [Fig. 5(b)]. KE distributions are given up to 1000 eV due to the difficulty in separating the signal corresponding to atomic emission with the prompt peak at higher kinetic energies. The most significant difference is observed for Al I, where the alloy Al I signal is shifted to lower KE values.

Maximum probable velocities for neutral atoms were calculated from OTOF profiles, with results given in Fig. 6(a) as a function of atomic mass. Similar to Figs. 3 and 4, the velocity distribution at FWHM is given as a shaded bar around the maximum probable velocity value. Velocities of neutral atoms from both pure metal and alloy targets decrease with increasing atomic

mass although the velocities from the alloy target appear more self-similar. Al neutral atoms show a large reduction in velocity in the alloy vs the pure metal LPP, while the other elements show smaller differences. Atom KEs are reported as a function of atomic mass in Fig. 6(b). The range of KEs at FWHM is represented as shaded bars around the maximum probable KE in Fig. 6(b). For all elements except Al, the most probable KEs are similar with respect to atomic mass and show small differences between pure elements and the alloy. For Al, the most probable KE is notably higher for the pure element vs the alloy. However, in the alloy, the Al KE is similar to the other elements. From velocity vs heat of vaporization and melting temperature for neutral atoms [Figs. 7(a) and 7(b), respectively], we find atom velocities also decrease with increasing heat of vaporization and melting temperature although the decay behavior varies between pure metal and alloy targets; a greater reduction in velocity is observed for neutral atoms in pure metal LPPs vs those in the multi-element (alloy) LPP.

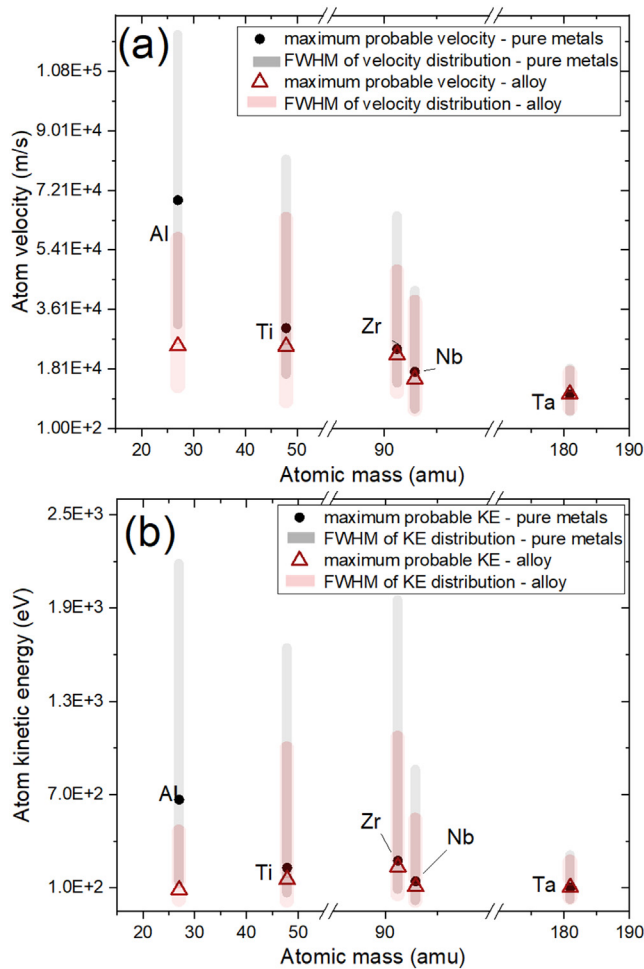


FIG. 6. (a) Velocity of neutral atoms from OTOF profiles (Fig. 5) from pure metal and alloy targets as a function of atomic mass. In (b), maximum probable KE of atomic species as a function of atomic mass are given. The distributions shown represent the velocity or KE distributions at FWHM.

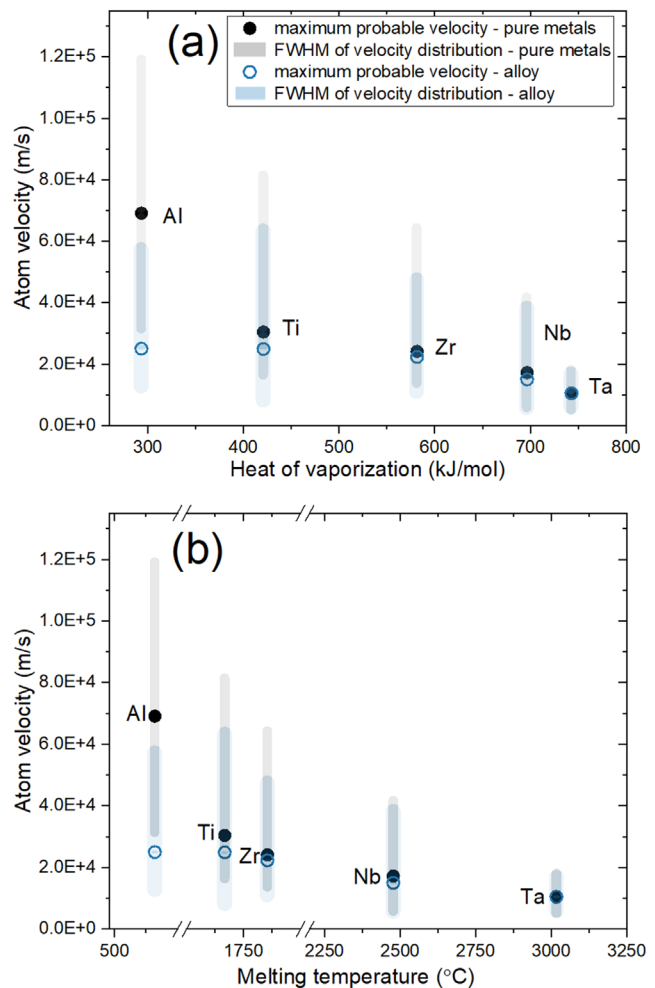


FIG. 7. Velocity of neutral atoms from pure metal and alloy targets as a function of (a) heat of vaporization (kJ/mol) and (b) melting temperature (°C).

11 April 2024 20:08:11

IV. DISCUSSION

The present study investigated ion and neutral atom kinetics in plasmas produced from pure vs multi-element (i.e., alloy) target materials using the Faraday cup and OTOF plasma diagnostic tools. The presence of multiple elements with varying properties in the plasma produced from the alloy target significantly impacts the kinetics of both ions and neutrals. We find several interesting trends in Faraday cup and OTOF signal data, including (i) the KE of ions are similar for all elements and the alloy although Al shows a slightly lower KE; (ii) the KE of ions are generally higher than neutral atoms, with the exception of Al; (iii) ion and neutral atom velocities decrease with increasing atomic mass, the heat of vaporization, and melting temperature; and (iv) neutral atom velocities are generally greater in plasmas produced from pure metal targets in comparison to the alloy LPP.

In the ion temporal profiles and KE distributions reported in Figs. 2(a) and 2(b), all ionic charge states are included and, therefore, contribute to the trends observed in velocity and KE distributions reported in Figs. 3 and 4. A particularly interesting observation is that the maximum probable KE for all ions [Fig. 3(b)] are similar, where the FWHM of all the KE distributions clearly overlap. However, Al KE is slightly lower than the most probable KE value for other targets, and this finding is likely attributed to the charge state distribution in Al vs other LPPs. The ionization energies of higher charge states for Al are much greater in comparison to other metals studied here; hence, the average charge state of the Al LPP is expected to be lower. This lower average ionization state can lead to the lower KE reported for Al, consistent with results from Torrisi *et al.*⁴⁰

With regard to the alloy target, there are many parameters that can influence alloy ion KE distributions, including the concentration of various elements present in the alloy.^{41,42} Ion energies and charge states in the alloy LPP are also impacted by ionization, acceleration, and recombination processes.⁴¹ When a weighted average atomic mass is estimated for the alloy target, the measured ion velocities and KE distributions agree well with trends for pure metal targets. To further investigate the impact of various ion charge states on the observed ion TOF profiles and KE distributions, a study employing charge-resolved analysis tools such as electrostatic energy analyzer (EEA),⁴³ time-of-flight mass spectrometer (TOF-MS),⁴⁴ Thomson parabola,⁴⁵ or retarding potential analyzer is required.^{36,46}

Another consideration when examining the difference between ion and neutral atom KE is the observation point where data were collected. The OTOF measurements of atomic emission temporal distributions were made at a distance of ≈ 6 mm from the target surface, while the ion TOF profiles were recorded at a distance of ≈ 18 cm from the target. Since all measurements were taken in a vacuum environment, the charge state of the ions will be frozen after a short distance from the target.²¹ We note that ions have greater kinetic energies than neutral atoms, with the exception of Al. In ns LPPs, the plasmas will be generated during the interaction of the leading edge of the laser pulse with the target, and the rest of the laser energy will be utilized for plasma heating through inverse bremsstrahlung (IB) absorption. During the IB absorption process, the energy will be absorbed by the electrons which thermalize with ions in a timescale (≈ 1 – 10 ps) faster than the duration of the laser pulse. Being lighter species, the electrons escape from the plasma followed by ions. A shift in ion KE profiles toward higher energies [Fig. 2(b)] indicates ion acceleration.

Results reported in Figs. 3 and 6 show that measured velocities for ions and neutral atoms decrease with increasing atomic mass, and this behavior is expected due to the relationship between KE, velocity, and atomic mass; for a constant KE, lighter elements will have a greater velocity relative to heavier elements. The observed decreasing ion velocity trends with increasing heat of vaporization and melting temperature (Figs. 4 and 7) suggest that the characteristics of ion emission from a ns LPP may be correlated with thermal properties of the target material.^{9,27} This correlation is consistent with the understanding that material removal via ns LA involves complex thermal phenomena, such as vaporization and phase explosion.⁴⁷ Measured velocities and KE of ions and neutral atoms have also been correlated with other parameters related to thermodynamic or material properties, such as electrical conductivity.²⁶

The similar observed KEs of neutral atoms in the plasma from the alloy target highlight the existence of a highly collisional plasma close to the target surface (i.e., in the Knudsen layer). LPPs are hotter and denser at early times and at closer distances from the target, and the species undergo significant collisions in the so-called Knudsen layer region.⁴⁸ The boundary of the Knudsen layer acts like a nozzle from which the plasma expands adiabatically. During adiabatic expansion, the velocities of ions/neutral atoms depend on mass (where velocity is proportional to $m^{-1/2}$). For the alloy plasma, collisions in the Knudsen layer act to produce similar KEs for all elements. For all plasmas, the kinetics of various species depends on initial plasma conditions. Given LA is performed in a vacuum, most of the collisions in the plasma occur at early times and at short distances from the target. The plasma expands adiabatically with the reduction in temperature and density as time progresses although at different rates for each target material.^{49,50}

Comparing the neutral atom OTOF profiles obtained from metal and alloy targets [Fig. 5(a)], significant differences are apparent, especially in the decay part of the temporal profiles. Differences in OTOF profiles for atomic transitions measured in plasmas produced from pure metal and alloy targets could be due to several factors, such as differences in number densities (number densities of neutral atoms are significantly lower in the case of the alloy target), collisional excitation and deexcitation in the Knudsen layer, charge transfer, ionization, recombination, and radiation trapping. For instance, the broad peak followed by a long tail observed in atom OTOF profiles [Fig. 5(a)] may be due to recombination of ions and electrons at later times in plasma expansion leading to the formation of neutral species. Recombination rate is dependent on charge state (Z), electron temperature (T_e), electron density (n_e), and ion density (n_i) according to the relation: $R_c \propto Z^3 \ln \sqrt{Z^2 + 1} T_e^{-9/2} n_e^2 n_i$.⁵¹ At lower plasma temperatures, which are reached at later times in plume expansion, recombination rates are higher and more favorable for the formation of neutral species. Having lighter mass, Al ions possess the highest maximum probable velocities, and fast neutrals can be formed by the recombination of fast ions with free electrons.⁵² However, for the alloy target, KEs for atoms are more similar which indicates the thermalization of various species in the plasma.

V. CONCLUSIONS

This article investigates the dynamics of ions and neutral atoms in LPPs generated via ns LA of Al, Ti, Zr, Nb, and Ta pure metals as compared to the results obtained from an alloy target comprising all of

these elements. We find that the maximum probable velocities of ions and neutral atoms decrease with increasing atomic mass, the heat of vaporization, and the melting temperature of the target material. There is a correlation between ion/neutral atom velocities and thermal properties, consistent with the understanding that ns LA is a thermally driven process.

Ion velocity for the alloy target agrees well with trends for pure metal targets, suggesting that the KE distribution represents an envelope where signals from each constituent element contribute. Al, however, does have a slightly lower maximum probable KE than ions from other target materials, which we attribute to a lower average charge state in the plasma. Ion acceleration is evident in LPPs, given that KEs from ions are higher than for neutrals (with the exception of Al); ion KE distributions have a forward bias; and temporal profiles show fast, low-intensity peaks for pure metal targets.

Velocities and KE of neutral atoms decrease with increasing atomic mass. When comparing velocities and KE of neutrals from pure vs alloy target materials, we find that values from the alloy target are more similar than those from pure metal targets. This trend may be attributed to collisions between species with different masses in the Knudsen layer. Such collisions reduce the KE of Al neutral atoms most significantly (and only minimally impact Ta atom KE) between single- and multi-element LPPs. Our findings also indicate that the properties and composition of the target material from which a LPP is generated strongly impact plume dynamics.

ACKNOWLEDGMENTS

This work was partially supported by the Department of Defense (DoD), Defense Threat Reduction Agency (DTRA) under Award No. HDTRA1-20-2-0001. P.K.D. was supported by the U.S. Department of Energy, Office of Science, and Office of Workforce Development for Teachers and Scientists (WDTS) under the Visiting Faculty Program (VFP). The content of the information does not necessarily reflect the position or the policy of the federal government, and no official endorsement should be inferred. Pacific Northwest National Laboratory is a multi-program national laboratory operated by Battelle for the U.S. Department of Energy under Contract No. DE-AC05-76RL01830.

AUTHOR DECLARATIONS

Conflict of Interest

M.C.P. is a part-time employee of a small business, Opticslah, LLC.

Author Contributions

Elizabeth J. Kautz: Conceptualization (equal); Data curation (lead); Formal analysis (lead); Investigation (lead); Methodology (equal); Visualization (lead); Writing – original draft (lead). **Mark C. Phillips:** Validation (equal); Visualization (supporting); Writing – review & editing (supporting). **Prasoon K. Diwakar:** Formal analysis (supporting); Writing – review & editing (supporting). **Alla Zelenyuk:** Writing – review & editing (supporting). **Sivanandan S. Harilal:** Conceptualization (equal); Funding acquisition (lead); Investigation (lead); Supervision (lead); Writing – review & editing (lead).

DATA AVAILABILITY

The data that support the findings of this study are available from the corresponding author upon reasonable request.

REFERENCES

- S. S. Harilal, M. C. Phillips, D. H. Froula, K. K. Anoop, R. C. Issac, and F. N. Beg, "Optical diagnostics of laser-produced plasmas," *Rev. Mod. Phys.* **94**, 035002 (2022).
- P. Yeates, J. T. Costello, and E. T. Kennedy, "The DCU laser ion source," *Rev. Sci. Instrum.* **81**, 043305 (2010).
- L. Poirier, D. J. Hemminga, A. Lassise, L. Assink, R. Hoekstra, J. Sheil, and O. O. Versolato, "Strongly anisotropic ion emission in the expansion of Nd:YAG-laser-produced plasma," *Phys. Plasmas* **29**, 123102 (2022).
- S. S. Harilal, B. E. Brumfield, N. L. LaHaye, K. C. Hartig, and M. C. Phillips, "Optical spectroscopy of laser-produced plasmas for standoff isotopic analysis," *Appl. Phys. Rev.* **5**, 021301 (2018).
- J. P. Singh and S. N. Thakur, *Laser-Induced Breakdown Spectroscopy* (Elsevier, Amsterdam, 2020).
- O. O. Versolato, "Physics of laser-driven tin plasma sources of EUV radiation for nanolithography," *Plasma Sources Sci. Technol.* **28**, 083001 (2019).
- H. Hutchinson, "Principles of plasma diagnostics," *Plasma Phys. Controlled Fusion* **44**, 2603 (2002).
- S. Irimiciuc, S. Gurlui, G. Bulai, P. Nica, M. Agop, and C. Focsa, "Langmuir probe investigation of transient plasmas generated by femtosecond laser ablation of several metals: Influence of the target physical properties on the plume dynamics," *Appl. Surf. Sci.* **417**, 108–118 (2017).
- A. Dogar, S. Ullah, H. Qayyum, Z. Rehman, and A. Qayyum, "Characterization of charge and kinetic energy distribution of ions emitted during nanosecond pulsed laser ablation of several metals," *J. Phys. D: Appl. Phys.* **50**, 385602 (2017).
- X. Wang, S. Zhang, X. Cheng, E. Zhu, W. Hang, and B. Huang, "Ion kinetic energy distributions in laser-induced plasma," *Spectrochim. Acta, Part B* **99**, 101–114 (2014).
- J. Singh, C. Fallon, P. Hayden, M. Mujawar, P. Yeates, and J. Costello, "Ion flux enhancements and oscillations in spatially confined laser produced aluminum plasmas," *Phys. Plasmas* **21**, 093113 (2014).
- J. S. Pearlman, "Faraday cups for laser plasmas," *Rev. Sci. Instrum.* **48**, 1064–1067 (1977).
- A. Raven, P. Rumsby, and J. Watson, "Multichannel digitizer for routine monitoring of ion emission from laser-driven implosions," *Rev. Sci. Instrum.* **51**, 351–354 (1980).
- J. Koch and D. Günther, "Review of the state-of-the-art of laser ablation inductively coupled plasma mass spectrometry," *Appl. Spectrosc.* **65**, 155A–162A (2011).
- V. Sivakumaran, H. Joshi, R. Singh, and A. Kumar, "Optical time of flight studies of lithium plasma in double pulse laser ablation: Evidence of inverse bremsstrahlung absorption," *Phys. Plasmas* **21**, 063110 (2014).
- M. Skočić, D. Dojić, and S. Bukvić, "Consideration of optical time of flight measurement in laser induced plasmas," *Spectrochim. Acta, Part B* **165**, 105786 (2020).
- E. J. Kautz, M. C. Phillips, A. Zelenyuk, and S. S. Harilal, "Oxidation in laser-generated metal plumes," *Phys. Plasmas* **29**, 053509 (2022).
- P. J. Skrodzki, M. Burger, I. Jovanovic, M. C. Phillips, B. E. Brumfield, J. Yeak, and S. S. Harilal, "Plume dynamics and gas-phase molecular formation in transient laser-produced uranium plasmas," *Phys. Plasmas* **26**, 083508 (2019).
- B. Verhoff, S. S. Harilal, and A. Hassanein, "Angular emission of ions and mass deposition from femtosecond and nanosecond laser-produced plasmas," *J. Appl. Phys.* **111**, 123304 (2012).
- A. Thum-Jager and K. Rohr, "Angular emission distributions of neutrals and ions in laser ablated particle beams," *J. Phys. D: Appl. Phys.* **32**, 2827 (1999).
- R. A. Burdt, Y. Tao, M. S. Tillack, S. Yuspeh, N. M. Shaikh, E. Flaxer, and F. Najmabadi, "Laser wavelength effects on the charge state resolved ion energy distributions from laser-produced Sn plasma," *J. Appl. Phys.* **107**, 043303 (2010).
- S. A. Irimiciuc, P.-E. Nica, M. Agop, and C. Focsa, "Target properties–plasma dynamics relationship in laser ablation of metals: Common trends for fs, ps and ns irradiation regimes," *Appl. Surf. Sci.* **506**, 144926 (2020).

- ²³E. J. Kautz, E. Ronnebro, A. Devaraj, D. Senor, and S. S. Harilal, "Detection of hydrogen isotopes in Zircaloy-4 via femtosecond LIBS," *J. Anal. At. Spectrom.* **36**, 1217 (2021).
- ²⁴D. Diaz and D. W. Hahn, "Plasma chemistry produced during laser ablation of graphite in air, argon, helium and nitrogen," *Spectrochim. Acta, Part B* **166**, 105800 (2020).
- ²⁵E. J. Kautz, E. N. Weerakkody, M. S. Finko, D. Curreli, B. Koroglu, T. P. Rose, D. G. Weisz, J. C. Crowhurst, H. B. Radousky, M. DeMagistris *et al.*, "Optical spectroscopy and modeling of uranium gas-phase oxidation: Progress and perspectives," *Spectrochim. Acta, Part B* **185**, 106283 (2021).
- ²⁶S. A. Irimiciuc, S. Chertopalov, M. Novotný, V. Craciun, and J. Lancok, "On the dynamics of transient plasmas generated by nanosecond laser ablation of several metals," *Materials* **14**, 7336 (2021).
- ²⁷N. Farid, S. Harilal, H. Ding, and A. Hassanein, "Kinetics of ion and prompt electron emission from laser-produced plasma," *Phys. Plasmas* **20**, 073114 (2013).
- ²⁸Y. Lin, M. He, W. Hang, and B. Huang, "Characterization of kinetic energy distributions of ions in high laser irradiance via orthogonal time-of-flight mass spectrometry," *Spectrochim. Acta, Part B* **76**, 197–202 (2012).
- ²⁹S. Alimpiev, M. Belov, V. Mlinsky, S. Nikiforov, and V. Romanjuk, "Negative-ion emission during laser ablation of multicomponent materials," *Appl. Phys. A* **58**, 67–72 (1994).
- ³⁰C. W. Schneider and T. Lippert, "PLD plasma plume analysis: A summary of the psi contribution," *Appl. Phys. A* **129**, 138 (2023).
- ³¹P. Willmott and J. Huber, "Pulsed laser vaporization and deposition," *Rev. Mod. Phys.* **72**, 315 (2000).
- ³²M. Cropper, "Thin films of alrcfeconicu high-entropy alloy by pulsed laser deposition," *Appl. Surf. Sci.* **455**, 153–159 (2018).
- ³³T.-W. Lu, C.-S. Feng, Z. Wang, K.-W. Liao, Z.-Y. Liu, Y.-Z. Xie, J.-G. Hu, and W.-B. Liao, "Microstructures and mechanical properties of CoCrFeNiAl_{0.3} high-entropy alloy thin films by pulsed laser deposition," *Appl. Surf. Sci.* **494**, 72–79 (2019).
- ³⁴V. Soni, B. Gwalani, T. Alam, S. Dasari, Y. Zheng, O. N. Senkov, D. Miracle, and R. Banerjee, "Phase inversion in a two-phase, bcc + b2, refractory high entropy alloy," *Acta Mater.* **185**, 89–97 (2020).
- ³⁵O. Senkov, C. Woodward, and D. Miracle, "Microstructure and properties of aluminum-containing refractory high-entropy alloys," *JOM* **66**, 2030–2042 (2014).
- ³⁶A. Thum-Jaeger, B. K. Sinha, and K. P. Rohr, "Time of flight measurements on ion-velocity distribution and anisotropy of ion temperatures in laser plasmas," *Phys. Rev. E* **63**, 016405 (2000).
- ³⁷S. Amoruso, M. Armenante, R. Bruzzese, N. Spinelli, R. Velotta, and X. Wang, "Emission of prompt electrons during excimer laser ablation of aluminum targets," *Appl. Phys. Lett.* **75**, 7–9 (1999).
- ³⁸S. Ratynskaia, G. Dilecce, and P. Tolia, "Nitrogen optical emission during nanosecond laser ablation of metals: Prompt electrons or photo-ionization?," *Appl. Phys. A* **117**, 409–413 (2014).
- ³⁹R. L. Kurucz, "The Kurucz Smithsonian atomic and molecular database," in *Astrophysical Applications of Powerful New Databases* (Smithsonian Astrophysical Observatory, Cambridge, MA, 1995), Vol. 78.
- ⁴⁰L. Torrisi, F. Caridi, D. Margarone, and A. Borrielli, "Plasma–laser characterization by electrostatic mass quadrupole analyzer," *Nucl. Instrum. Methods Phys. Res., Sect. B* **266**, 308–315 (2008).
- ⁴¹M. R. Bedilov, Y. A. Bykovskiĭ, D. Kuramatov, A. Kholbaev, and K. Khaitbaev, "Investigation of the formation and flight of silver ions in a multicomponent laser plasma," *Sov. J. Quantum Electron.* **17**, 1068 (1987).
- ⁴²M. Bedilov, Y. A. Bykovskiĭ, D. Kuramatov, and K. Khaitbaev, "Interaction of laser radiation with matter. Laser plasma: Dependences of the energy spectra of gold and silver ions on their concentration in a multicomponent laser plasma," *Quantum Electron.* **21**, 71–73 (1991).
- ⁴³S. Amoruso, M. Armenante, V. Berardi, R. Bruzzese, G. Pica, and R. Velotta, "Charged species analysis as a diagnostic tool for laser produced plasma characterization," *Appl. Surf. Sci.* **106**, 507–512 (1996).
- ⁴⁴D. Wu, L. Zhang, P. Liu, L. Sun, R. Hai, and H. Ding, "Diagnostic study of laser-produced tungsten plasma using optical emission spectroscopy and time-of-flight mass spectrometry," *Spectrochim. Acta, Part B* **137**, 70–76 (2017).
- ⁴⁵L. Torrisi, M. Cutroneo, L. Andò, and J. Ullschmied, "Thomson parabola spectrometry for gold laser-generated plasmas," *Phys. Plasmas* **20**, 023106 (2013).
- ⁴⁶M. Haider, A. Shaim, and H. Elsayed-Ali, "Characterization of laser-generated aluminum plasma using ion time-of-flight and optical emission spectroscopy," *J. Appl. Phys.* **122**, 203301 (2017).
- ⁴⁷A. H. Lutey, "An improved model for nanosecond pulsed laser ablation of metals," *J. Appl. Phys.* **114**, 083108 (2013).
- ⁴⁸W. Pietsch, "Effect of Knudsen-layer formation on the initial expansion and angular distribution of a laser-produced copper plasma at reduced pressure of air," *J. Appl. Phys.* **79**, 1250–1257 (1996).
- ⁴⁹S. A. Irimiciuc, S. Chertopalov, J. Bulf, M. Vondracek, L. Fekete, P. Jiricek, M. Novotný, V. Craciun, and J. Lancok, "Insight into the plasma oxidation process during pulsed laser deposition," *Plasma Processes Polym.* **19**, e2100102 (2021).
- ⁵⁰E. R. Wainwright, F. De Lucia, T. P. Weihs, and J. L. Gottfried, "Spatiotemporal and emission characteristics of laser-induced plasmas from aluminum-zirconium composite powders," *Spectrochim. Acta, Part B* **183**, 106270 (2021).
- ⁵¹J. Freeman, S. Harilal, B. Verhoff, A. Hassanein, and B. Rice, "Laser wavelength dependence on angular emission dynamics of Nd:YAG laser-produced Sn plasmas," *Plasma Sources Sci. Technol.* **21**, 055003 (2012).
- ⁵²N. Smijesh, K. Chandrasekharan, and R. Philip, "Acceleration of neutrals in a nanosecond laser produced nickel plasma," *Phys. Plasmas* **21**, 123507 (2014).